

Detection of low-frequency breaks in power density spectrum of GX 339-4 in faint low/hard state observations using AstroSat data

Nazma Husain,^{1*} Ranjeev Misra,² Somasri Sen¹

¹*Department of Physics, Jamia Millia Islamia, New Delhi-110025, India*

²*Inter-University Centre for Astronomy and Astrophysics, Pune-411007, India*

Accepted XXX. Received YYY; in original form ZZZ

ABSTRACT

We present the spectro-timing analysis of the black hole binary system GX 339-4 using AstroSat data extracted at the beginning of outbursts in 2017 and 2019. The joint spectral fitting of LAXPC and SXT data revealed that the source was in a faint low/hard state for both 2017 and 2019 observations with a nearly equal photon index of ~ 1.57 and ~ 1.58 and with Eddington ratio, L/L_{Edd} , of 0.0011 and 0.0046 respectively. The addition of a reflection component into the spectral modelling improved the fit ($\Delta\chi^2 \approx 6$ for 2017 and $\Delta\chi^2 \approx 7$ for 2019), pointing towards the presence of weak reflection features arising due to irradiation of the accretion disk. The power density spectrum (PDS) consisted of strong band-limited noise with a break at low frequencies, described with a broken power-law model and a combination of few zero-centered Lorentzian. With Lorentzian fitting the break was detected at ~ 6 mHz for 2017 and at ~ 11 mHz for 2019 observation which is almost a factor of two higher than those obtained with broken power-law fitting. Detection of this characteristic frequency is validated by results from independent detectors (LAXPCs and SXT). The break frequency is roughly consistent with results from earlier observations that showed an evolution of the frequency with flux, which is in accordance with the truncated disk model. Associating the break frequency with viscous time scale of the accretion disk, the truncation radius was estimated to be ~ 93 gravitational radius for 2017 and ~ 61 gravitational radius for 2019 observation.

1 INTRODUCTION

A Black hole X-ray binary system (BHXB) is a system consisting of a black hole and a companion star orbiting about their common centre of mass. The black hole due to its gravitational field accretes matter from the orbiting star via Roche-lobe overflow mechanism or stellar wind depending upon the mass of the companion star. Infalling matter has significant angular momentum which allows for the formation of an accretion disk around the black hole. This disk is luminous in X-rays in the vicinity of the compact object. Another component of flow exists near the compact object which is hotter and optically thinner than the disk and is responsible for the hard X-ray emission known as hot inner flow (Sunyaev & Trümper 1979; Thorne & Price 1975). The exact geometry of this flow is still under discussion. Till now, many Galactic black hole binaries have been detected and analysed amongst which GX 339-4 (V821 Ara) remains one of the most extensively observed low mass BHXB system due to its variety of spectral states and complex outburst profile. The accretion of matter in this source is dominated by Roche-lobe overflow mechanism due to its low mass companion star (Heida et al. 2017). Since its discovery in 1973 by satellite OSO-7 (Markert et al. 1973), frequent outbursts have been observed every 2-3 years consistent with its transient nature. During these outbursts, GX 339-4 manifests spectral and temporal transitions which may depend on the geometry and luminosity of the two accretion flows (Gilfanov 2010).

describe different states of the binary system, with each state exhibiting different spectral and timing properties. The distinction between the states is explained in Belloni (2006, 2010). Many black hole transients including GX 339-4 follow a q-shaped HID (Homan & Belloni 2005; Dunn et al. 2010) during their complete outburst. In beginning of the outburst, the source starts in the low/hard state (LHS) with a dominating power-law component (photon index, $\Gamma < 2$) originating from the inner hot flow. As the luminosity increases, the source transits to the Hard Intermediate State (HIMS) which is a softer state ($\Gamma > 2$) and has an increased amount of disk contribution to the spectrum but with little change in its timing properties as compared to the low/hard state. Further along the outburst, the source evolves into the Soft Intermediate State (SIMS) with further softening of the spectrum and significant change in timing properties. From the SIMS the source then transits to the Soft state (SS) which has dominating disk emission modelled by a disk multi-color black body spectrum. Similar trend is followed during the decline of the outburst but in reverse order, hence putting the source back into the low/hard state, completing the q-shaped HID.

One of the ways to understand the accretion flow in strong gravitational field is to study the timing variability of the flow. A common technique for X-ray timing analysis is to study the Fourier transform of the X-ray flux, also expressed in terms of Power Density Spectrum (PDS) (Van der Klis 1989). With changing states the PDS has been observed to show different components. In low/hard state the PDS consists of a strong band-limited noise

Different locations on the Hardness Intensity Diagrams (HID)

(BLN) continuum (Oda et al. 1971) with a break at low frequency (Titarchuk et al. 2007) and sometimes accompanied with a low-frequency Quasi-Periodic Oscillation (QPO). The PDS in this state is usually fitted with a few broad Lorentzians or a broken power-law model (Belloni et al. 2002; Stiele & Kong 2017; Nowak 2000). As the source rises in luminosity and moves towards softer states the rms variability reduces and prominent type-B (~ 5 -6 Hz) and type-C (~ 0.1 -15 Hz) QPOs are observed, see for *e.g.* Casella et al. (2005).

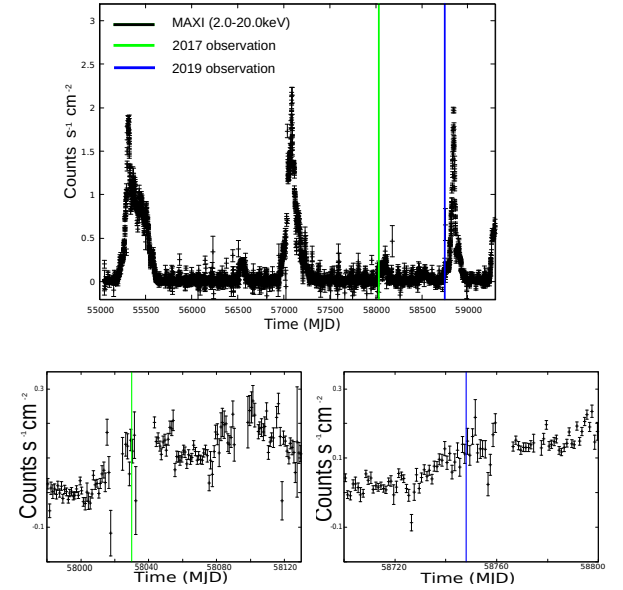
The band-limited noise detected in low/hard state has a characteristic low-frequency break (ν_{brk}) which has been observed to vary during the cycle of outburst. In νP_ν representation, where P_ν is the normalized power, the break characterises the PDS such that below this the power spectrum is a power-law of index -1 and above the break it takes the shape of a flattened power-law (Miyamoto et al. 1992; Belloni & Hasinger 1990). This low-frequency break has been previously detected in the PDS of GX 339-4 in several studies. For *e.g.*, Nowak et al. (1999b) studied the low luminosity RXTE observations of GX 339-4, and detected a break frequency at ~ 30 mHz. Ford et al. (1998) detected a break at 70 mHz for one of the hard state observations of 1997 outburst for GX 339-4. Migliari et al. (2005) also studied this outburst and detected the low-frequency break in frequency range 37 to 107 mHz for its hard state observations. Nandi et al. (2012) performed a detailed analysis of 2010-2011 outburst of this source and observed the break frequency in different states amongst which the only hard state observation exhibited a break at 880 mHz. Similarly, Stiele & Yu (2015) analysed two hard state observations of GX 339-4 extracted in 2004 and 2009 and found low-frequency breaks at 44.7 and 8.7 mHz respectively. Also, break frequencies in the low luminosity state were detected using NuSTAR data for 2015 outburst by Stiele & Kong (2017) in range 30-70 mHz.

In addition to these detections, Wijnands & van der Klis (1999) studied the aperiodic variability of multiple BHXBs including GX 339-4, Cyg X-1, XTE J1748-288, GRO J1655-40 and few others in hard state. They detected the break for GX 339-4 in the range 40-64 mHz. They have also observed a positive correlation between the low-frequency QPO (ν_{QPO}) and the low-frequency break (ν_{brk}) such that $\nu_{QPO} \sim 5 \nu_{brk}$, which implies that both band-limited noise and low-frequency QPO might have a common physical origin. Furthermore, Plant et al. (2015) showed that as GX 339-4 progresses through the hard state, the low-frequency break in the PDS exhibits a trend of moving towards higher frequencies. They detected a 2.55 mHz break for their lowest flux observation in the hard state and observed an evolution of the inner disk radius (R_{in}) such that it moved towards the Inner most Stable Circular Orbit (ISCO) as the source flux increased.

Such low-frequency breaks in the PDS have been detected for other black hole systems as well. For *e.g.*, Radhika et al. (2014) studied the BHXB system MAXI J1836-194 during its outburst showing the evolution of ν_{brk} from 300-1200 mHz in its rise from low/hard state to soft state. Cygnus X-1 exhibited ν_{brk} at frequency 170 mHz in work by Nowak et al. (1999a) and at 200 mHz in work by Belloni et al. (1996), GRO J1655-240 showed strong band-limited noise along with break at frequencies ~ 100 -1000 mHz in Méndez et al. (1998). For GX 339-4, the break frequency has been usually detected above 10 mHz, as there are very few low flux observations of this source on which detailed timing studies are performed.

In this work, we present the spectro-timing analysis of faint low/hard observations of GX 339-4 at the beginning of 2017 and

Figure 1. MAXI lightcurve for GX 339-4 in energy range 2.0-20.0 keV from June, 2009 to March, 2021 along with the zoomed in lightcurves for both AstroSat observations (Here, the vertical lines represents the AstroSat observations on 4th and 5th of Oct, 2017 (green) and on 22nd and 23rd of Sept, 2019 (blue))



2019 outbursts. The layout of this paper is as following: In section 2, we mention the various parameters of the source GX 339-4. In Section 3, we explain the selected AstroSat observations and reduction of data for payloads LAXPC and SXT. In Section 4, we discuss the spectral and timing analysis. Lastly, in Section 5 we summarise and discuss the obtained results.

2 PARAMETERS OF GX 339-4

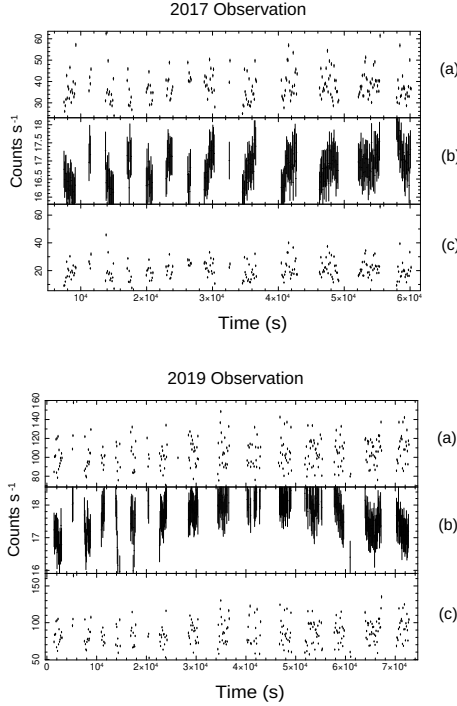
Heida et al. (2017) analysed the absorption lines detected in the Near Infrared (NIR) spectrum from the donor star (K-type), when the source GX 339-4 was in its quiescent state. They estimated a mass function of $f(M) = 1.91 \pm 0.08 M_\odot$ by measuring the projected rotational velocity and radial velocity curve semi-amplitude of this donor star. The upper and lower limits to the mass of the black hole were set to $2.3 M_\odot \leq M \leq 9.5 M_\odot$. Hynes et al. (2004) estimated a distance of GX 339-4 to be $6 \leq d \leq 15$ kpc after studying the optical spectra of Na and Ca lines along the line of sight of the source. Also, Zdziarski et al. (2019) constructed the evolutionary models of the donor star of GX 339-4 and compared it with its observed data. They estimated the inclination to be between values $\sim 40^\circ - 60^\circ$. Similarly, in Heida et al. (2017), the upper limit of inclination was set to $< 78^\circ$ as the binary does not show eclipses in X-ray lightcurve and the lower limit on the inclination was set to 37° because of the upper limit on $M \leq 9.5 M_\odot$.

In this work, we have assumed the mass of the black hole to be, $M = 6 M_\odot$ and distance, $d = 8$ kpc with inclination of the binary fixed at 60° .

3 ASTROSAT OBSERVATIONS AND DATA REDUCTION

AstroSat is India's first multi-wavelength astronomical satellite, it was launched in Sept, 2015. It has five major components ascribing

Figure 2. (a) Total count rate of source with background (b) Background (c) Background subtracted source count rate for 2017 (top) and 2019 (bottom) observations.



to different energy ranges of the electromagnetic spectrum among which Large Area X-ray Proportional Counter (LAXPC) and Soft X-ray Telescope (SXT) provide opportunity to study X-ray emission in energy ranges 3.0-80.0 keV and 0.3-8.0 keV respectively (Yadav et al. 2016; Agrawal et al. 2017a).

The source GX 339-4 exhibits outburst every 2-3 years amongst which some outbursts fail to show state transitions and remain in the low/hard state. The source was in the course of one such failed outburst in September 2017, when after staying in quiescence since 2016, the source re-brightened and was observed by Faulkes telescope (Russell et al. 2017a). Follow up observations were conducted by XRT/SWIFT (Gandhi et al. 2017) and Australia Telescope Compact Array (ATCA) (Russell et al. 2017b). Later on, AstroSat observed it at the initial stage of this outburst on 4th and 5th of Oct, 2017 (Observation ID: A04_109T01_9000001578) with an exposure time of ~60 ks. The source again re-brightened in August 2019 (Rao et al. 2019) following which AstroSat observed it on 22nd and 23th of Sept, 2019 (Observation ID: A05_166T01_9000003192) with an exposure time of ~35 ks. This observation was also extracted at the beginning of the outburst. The MAXI light curve for the source in energy range 2.0-20.0 keV is shown in Figure 1 with simultaneous AstroSat observations represented as vertical lines. We did not consider early AstroSat observations of the source in this work due to their significantly lower values of LAXPC count rates of < 3 counts s⁻¹ as compared to 22 and 86 counts s⁻¹ for 2017 and 2019 observation respectively. Here, in Figure 2, we plot the total count rate of source with background, background and background subtracted source count rate using LAXPC20 data for both observations in energy range 3.0-20.0 keV. We have analysed the data from LAXPCs and SXT and the reduction of their data-sets is discussed in the next section.

3.1 Large Area X-ray Proportional Counter(LAXPC)

LAXPC has three identical proportional counters LAXPC10, 20 and 30. LAXPC30 was switched off earlier on 8th March, 2018 because of abnormal gain changes <http://astrosat-ssc.iucaa.in/>. LAXPC provides a large effective area for energies 3.0-80.0 keV (~ 6000 cm²) and high time resolution of 10 μ s (Agrawal et al. 2017b). Level 1 data for both 2017 and 2019 observations were downloaded from AstroSat archive. These observations were conducted in Event mode which records data with information about the arrival time and energy of each incoming photon. Reduction of level 1 raw data to level 2 data was completed with the LAXPC software (version as of May, 2018) available on <http://astrosat-ssc.iucaa.in/?q=laxpcData>. Due to the low count rate of both observations, see Figure 2, the background lightcurves and spectra were generated using the Fortran codes for Faint sources in LAXPC software. The lightcurve and spectra were obtained using "laxpc_make_lightcurve" and "laxpc_make_spectra" codes.

3.2 Soft X-ray Telescope(SXT)

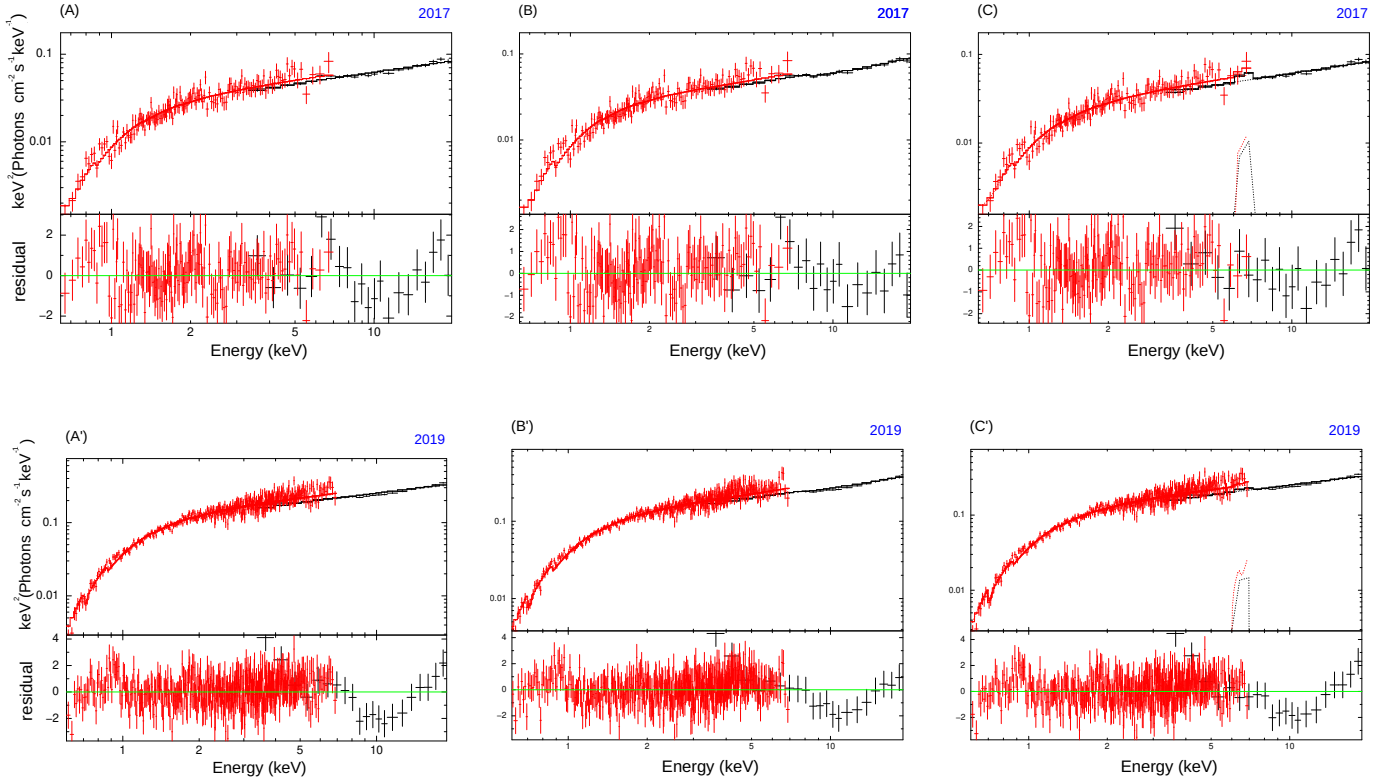
SXT observes low energy or softer X-rays in energy range 0.3-8.0 keV with high sensitivity. This payload has a Wolter I optics geometry arrangement of reflecting mirrors and an X-ray CCD, which provides an effective area of approximately 90 cm² at ~ 1.5 keV (Singh et al. 2017). The level 2 data for SXT was downloaded from AstroSat archive in Photon Counting mode (PC). The reduction of data was achieved with tools provided by SXT team at TIFR (https://www.tifr.res.in/~astrosat_sxt/dataanalysis.html). All individual clean event files for all orbits were merged with SXT_EVENT_MERGER tool for each data set. The image of the source was extracted using the merged eventfile and a circular region of radius 15 arcmin centered on the source was considered for further data analysis. Also, latest RMF (sxt_pc_mat_g0to12.rmf) and Background (Sky-Bkg_comb_EL3p5_Cl_Rd16p0_v01.pha) files were used. The ARF file (sxt_pc_excl00_v04_20190608.arf) given by the SXT team was corrected for the vignetting effect using the SXT_ARF_TOOL. The spectrum for SXT was extracted using the HEASoft (version 6.26.1) package XSELECT. The SXT spectrum was further grouped with the background, RMF and corrected ARF files by the interactive command 'grppha' producing the final SXT spectrum.

4 ANALYSIS AND RESULTS

4.1 Spectral Analysis

The spectrum of most black hole binaries has been observed to have three major components with varying contribution during different spectral states (Hard or soft states), first is multi-color black body radiation emitted from the surface of the thin optically thick accretion disk, second is comptonization spectrum from the inner hot flow where the seed photons from the disk get Compton scattered by the high energy electrons in the Compton cloud giving the hard spectrum and lastly the reflection spectrum, where the contribution comes from the irradiation of accretion disk by these comptonized photons giving rise to absorption and emission features such as Fe k α line in range 6.4-6.7 keV and Compton hump peaking at ~30 keV. Since, the skewness and broadening of such reflection features seen in the spectrum are induced by the relativistic effects occurring in the vicinity of the compact object, therefore these features in turn allow to probe the region of strong

Figure 3. The joint photon spectrum with ratio of data to model plot for GX 339-4 in energy range 0.6-20.0 keV for 2017 observation (upper panel) with models (A) $TBabs*Powerlaw$ (B) $TBabs*Ireflect*Powerlaw$ (C) $TBabs*(Powerlaw+Relline)$ and for 2019 observation (bottom panel) with models (A') $TBabs*Powerlaw$ (B') $TBabs*Ireflect*Powerlaw$ (C') $TBabs*(Powerlaw+Relline)$



gravity.

For spectral analysis, we considered joint fitting of data from LAXPC20 and SXT, this fitting allows the same model to fit two data files simultaneously. Only LAXPC20 data was used for spectral fitting because of its better constraint on the background. For each observation, the common usergti was created for payloads LAXPC20 and SXT. This usergti was then used to create the spectrum for LAXPC20 in energy range 3.0-20.0 keV (for >20.0 keV the background dominates the spectrum notably) and the spectrum of SXT in energy range 0.6-7.0 keV. The parameters for all the selected models were tied for data from the payloads LAXPC20 and SXT. A constant factor was used to account for the two different detectors. Also, for all fittings a 3% of systematic error was considered.

In the low/hard state, the continuum is dominated by comptonized spectrum, therefore the first model we fit to the photon spectrum for both observations is an absorbed power-law (XSPEC model $TBabs*Powerlaw$) to the joint spectrum of LAXPC20 and SXT in total energy range of 0.6-20 keV. Here, the model component $TBabs$ accounts for the intergalactic absorption of the incoming photons from the source, N_H gives the column density in units of 10^{22} cm^{-2} . We let this parameter vary in the fit. The fitted model parameters along with Reduced $\chi^2 = \chi^2/dof$, where dof is the degrees of freedom, are given in Table 1. The fit shows that the continuum for both observations could be described by the absorbed power-law model. The photon index takes value < 2 for both observations (~ 1.57 for 2017 and ~ 1.58 for 2019) which implies that during these observations the source was in the hard state, which is expected for this

source as these observations were extracted at the beginning of the two outbursts.

After fitting the spectra with absorbed power-law, some residuals still remain in the data to model ratio. Therefore, the next model we fit the joint spectrum is $Ireflect$ convolved with $Powerlaw$ (XSPEC model $TBabs*Ireflect*Powerlaw$). Reflection model $Ireflect$ is a generalisation of model $Pexriv$, XSPEC (Magdziarz & Zdziarski 1995). This model accounts for the edge absorptions and ignores the line emissions such as the Fe line. In this model combination, the abundances of Fe and other elements were set to solar values. We also assume the temperature of accretion disk to be 30,000 K and since the ionization parameter was not well constrained therefore we fix it to a large value of 900. The best fit values of parameters for both observations are given in Table 1.

Applying the above model to the spectral modelling improved the fit with $\Delta\chi^2 \sim 6$ for 2017 observation and $\Delta\chi^2 \sim 7$ for 2019 observation but residuals in the iron line region persist therefore we use another model combination consisting of reflection component $Relline$ (Dauser et al. 2010) (XSPEC model $TBabs*(Powerlaw+Relline)$). One of the most prominent features seen in the reflection spectrum of black hole binary system is Fe $K\alpha$ line in region 6.4-6.7 keV (depending upon the ionization of Fe in the disk). $Relline$ applies appropriate relativistic broadening effects to the Fe $K\alpha$ line after assuming an intrinsic zero width for the line emission. We fit the model $TBabs*(Powerlaw+Relline)$ to the joint spectrum of LAXPC20 and SXT. The emissivity indices for both inner and outer disk were set to 3 (Emissivity depends on radius R as $\epsilon \propto R^{-3}$) which is an assumed value for Newtonian

Table 1. Best fit values of spectral parameters for both observations of 2017 and 2019 with models *TBabs*Powerlaw* (Top Panel), *TBabs*Ireflect*Powerlaw* (Middle Panel) and *TBabs*(Powerlaw+Relline)* (Bottom Panel) along with the Eddington ratio for each model

Model	Parameter	2017	2019
TBABS	N_H (10^{22} cm^{-2})	$0.430^{+0.035}_{-0.033}$	$0.440^{+0.014}_{-0.014}$
POWERLAW	Γ	$1.570^{+0.031}_{-0.031}$	$1.583^{+0.020}_{-0.020}$
	N_Γ (10^{-2})	$2.35^{+0.17}_{-0.15}$	$9.73^{+0.45}_{-0.43}$
χ^2/dof		189.61/169.00 = 1.12	531.82/441.00 = 1.21
L/L_{edd} %		0.114	0.463
TBABS	N_H (10^{22} cm^{-2})	$0.490^{+0.050}_{-0.047}$	$0.460^{+0.022}_{-0.021}$
POWERLAW	Γ	$1.680^{+0.080}_{-0.077}$	$1.640^{+0.043}_{-0.042}$
	N_Γ (10^{-2})	$2.68^{+0.30}_{-0.27}$	$10.30^{+0.66}_{-0.62}$
IREFLECT	RS	$0.50^{+0.45}_{-0.35}$	$0.27^{+0.22}_{-0.19}$
χ^2/dof		183.55/168.00 = 1.09	524.99/440.00 = 1.19
L/L_{edd} %		0.115	0.464
TBABS	N_H (10^{22} cm^{-2})	$0.410^{+0.034}_{-0.033}$	$0.440^{+0.014}_{-0.014}$
POWERLAW	Γ	$1.550^{+0.032}_{-0.032}$	$1.58^{+0.02}_{-0.02}$
	N_Γ (10^{-2})	$2.31^{+0.17}_{-0.15}$	$9.59^{+0.46}_{-0.44}$
RELLINE	N_{Rell} (10^{-4})	$2.31^{+1.06}_{-1.03}$	$3.77^{+3.2}_{-3.1}$
χ^2/dof		175.60/168.00 = 1.05	522.67/456.00 = 1.15
L/L_{edd} %		0.110	0.460

Notes : 1) The errors were calculated in 90 % confidence region.

2) RS is reflection scaling factor .

3) Eddington ratio (L/L_{edd} %) was calculated using *cflux* model in energy range 0.6-10.0 keV.

accretion disks (Fabian et al. 1989; Laor 1991). We fix the outer radius of disk to $1000 R_g$, where R_g is the gravitational radius (GM/c^2). Since the fit was insensitive to the value of spin therefore we fixed it to value 0.9. After including this reflection component in the model the $\Delta\chi^2$ improved further by ~ 8 for 2017 observation and by ~ 2 for 2019 observation. As the χ^2 fit was insensitive to different values of R_m in *Relline* component therefore it was fixed to $100 R_g$ for both observations. The respective fit parameters are mentioned in Table 1. There are residuals in the LAXPC spectrum for the 2019 observation, which could either be due to a slight underestimation of the systematic uncertainty in the response (3% has been assumed here) or a physical component. We note that the addition of an absorption edge at 8.5 keV (perhaps due to iron) and with a depth of ~ 0.23 significantly reduces the residuals and improves the fit, $\Delta\chi^2 \sim 45$. However, given the uncertainty in the LAXPC response, we are not sure about the physical origin of the edge. We note that the addition of the component does not lead to any significant change in the value of the power-law index or the flux level. Furthermore, we also fit two other commonly used reflection components *Xillver* and *Reflionx* and we do not mention the best fit values as the $\Delta\chi^2$ did not improve further for both observations.

4.2 Timing Analysis

In order to study the variability of the source GX 339-4, we utilized the broadband Power density spectrum. For the timing analysis of the source we created the PDS using the HEASoft tool POWSPEC <https://starchild.gsfc.nasa.gov/xanadu/xronos/help/powspec.html>. For 2017 observation, the PDS was generated for LAXPC10 and LAXPC20 individually and combined. In POWSPEC, the PDS was created from 0.1 s binned background subtracted lightcurve in the energy range 3.0-20.0 keV. The lightcurve was divided into 35 segments with length of each segment as 1.64 ks. Geometric rebinning was undertaken to smoothen the PDS. These segments were then averaged producing the final PDS of the observation. Also, the normalization is such that the PDS can be expressed in units of rms^2/Hz . Similarly for 2019 observation, the PDS was generated from 0.1 s binned background subtracted lightcurve in the energy range 3.0-20.0 keV for LAXPC20 detector only. The lightcurve was divided into 44 segments with length of each segment to be 1.64 ks. Geometric rebinning was undertaken to smoothen the PDS. Similar to 2017 observation, the normalization is such that the PDS can be expressed in units of rms^2/Hz .

Further, the PDS of the source with SXT data was generated from 2.3775 s binned (since it's the minimum time-bin value for SXT) background subtracted lightcurve in the energy range 0.6-7.0 keV. The lightcurve was divided into 44 and 59 segments for 2017 and 2019 observations respectively. Each segment was of

length 0.512 ks. Geometrical rebinning was considered to smoothen the PDS. These segments were then averaged producing the final PDS of each observation.

The characteristic PDS in hard state has a broadband noise continuum with a break at low frequency below which the νP_ν curve has power-law index -1 i.e. $\nu P_\nu \propto \nu^{-(-1)}$, and above which it takes the form of an almost flattened power-law after noise subtraction i.e. $\nu P_\nu \propto \nu^0$. For fitting the PDS we considered two different models (1) a broken power-law model with different power-law indices for above and below the low-frequency break (ν_{brk}), P_1 for $< \nu_{brk}$ and P_2 for $> \nu_{brk}$ and (2) a combination of few zero-centered Lorentzians ($L(\nu)$) with peak frequency ν_L (i.e. the frequency at which νP_ν peaks) and normalization N_L for each component. A constant was implemented to fit the Poissons noise (N_{noise}).

The fitting of νP_ν curves with both models are plotted in Figure 4 and 5. The best fit values of parameters are mentioned in Table 2 and Table 5 along with the reduced χ^2 . For Model 1 fitting, the power-law index P_1 was fixed at 0.0 because of its ill constrain when kept as a free parameter and since it is established from previous observations of GX 339-4 that below the break νP_ν can be well fitted with a power-law with index 0.0 in hard state. As it is evident that for 2017 observation, LAXPC10 and LAXPC20 data have nearly equal values for parameters N_{Bkn} and P_2 respectively, which led us to perform combined timing analysis for LAXPC10 and LAXPC20 as well. As for the SXT fitting, P_2 could not be well constrained therefore it was fixed equal to the value obtained for LAXPC10 and LAXPC20 combined. Similarly, for 2019 observation P_2 for SXT was fixed to that found for LAXPC20. For Model 2 fitting, three zero-centered Lorentzians were used to describe the LAXPC PDS. However, only two Lorentzian components were used to fit for SXT data, since the third component used for the LAXPC PDS fitting, peaked at a frequency higher than the SXT frequency range. Moreover, the frequency of the second component for SXT was fixed at the value obtained from the LAXPC fit. The peak frequency of the first component is about a factor of two higher than the break frequency obtained from the broken power-law fit.

In both panels of Figure 6, we plot this peak frequency of the first Lorentzian component (which we also refer to as the "break" frequency) as a function of the unabsorbed flux in the 0.6 - 10 keV band. Selection of this energy band allowed us to compare our results with those obtained by Plant et al. (2015), who have reported variation of break frequency with the unabsorbed flux in the 0.5-10 keV range for the low hard state observation of GX 339-4. The top panel of Figure 6 shows that the results obtained in the work are consistent with the trend observed by Plant et al. (2015). Nandi et al. (2012) have reported break frequency for six observations of which one of them is in the hard state, while the others are in the soft or intermediary states. For the hard state observation, we used the spectral parameters mentioned to estimate the flux in 0.6-10 keV band and found that the break frequency is significantly higher than the value reported by Plant et al. (2015) for similar flux levels, but it maybe noted that their observation was just before a transition to the soft state and had a relatively high inner disk temperature of ~ 1.3 keV. The break frequencies and flux values reported by Stiele & Yu (2015) (flux values in 0.6-10 keV has been estimated using their reported spectral parameters) are closer to the values obtained by Plant et al. (2015). Migliari et al. (2005) have also presented estimates of the break frequencies for GX 339-4, however they do not tabulate the spectral parameters but instead give absorbed flux values in 3-9 keV band. If we assume that the flux in the 0.6-10 keV band are about a factor of two to three times higher, then their values are consistent with those obtained by Plant et al. (2015) and this work. Stiele

& Kong (2017) used a complex model to fit the spectral parameters and reported the 0.8-78 keV flux values. Again, if we assume that the flux in the 0.6-10 keV is about a factor of two or three lower then they would be consistent. Belloni et al. (2005) have reported break frequencies but not the corresponding flux values and hence we cannot make a comparison. The lower panel of Figure 6 shows these values quoted from literature along with the AstroSat results.

5 SUMMARY AND DISCUSSION

We have analysed the black hole candidate GX 339-4 when it was at the beginning of its outbursts in 2017 and 2019. For 2017 observation, the joint spectral analysis of LAXPC and SXT showed that an absorbed power-law could well describe the photon spectrum with photon index, $\Gamma = 1.57$ and column density, N_H (10^{22} cm^{-2}) = 0.43. It was in faint low hard state as the unabsorbed flux in energy range 0.6-10.0 keV was only $1.17 \times 10^{-10} \text{ erg s}^{-1} \text{ cm}^{-2}$ with Eddington ratio of 0.11 %. The spectrum consisted of weak reflection features such as Fe $K\alpha$ line and beginning of Compton hump, therefore modelling the reflection emission with two different reflection models *Ireflect* and *Relline* improved the χ^2 fit. XSPEC model *Ireflect*, assumes reflection from an ionized accretion disk whereas *Relline* applies the relativistic effects to the iron line.

Similar results were found for 2019 observation as the photon spectrum was modelled by an absorbed power-law with $\Gamma \sim 1.58$ and N_H (10^{22} cm^{-2}) = 0.44. The source was in the faint low/hard state in this observation as well, since the unabsorbed flux was found to be ~ 4 factor higher ($4.72 \times 10^{-10} \text{ erg s}^{-1} \text{ cm}^{-2}$) than 2017 observation with Eddington ratio of 0.46 percent. This observation was also modelled with reflection components *Ireflect* and *Relline* leading to improvement in χ^2 fit.

The timing study of GX 339-4 was accomplished using the Fourier transformation technique. The PDS of both observations were fitted with a broken power-law model and multi-Lorentzian model. Each of the two fittings gives a mHz break in the PDS of both the observations. The 2017 observation shows a break at $\sim 3 \text{ mHz}$ with broken power-law fitting and at $\sim 6 \text{ mHz}$ with Lorentzian fitting for LAXPC20. The detection of this mHz break is validated from three independent detectors LAXPC10, LAXPC20 and SXT. The 2019 observation shows a break at $\sim 5 \text{ mHz}$ with broken power-law fitting and $\sim 11 \text{ mHz}$ with Lorentzian fitting for LAXPC20. Detection of this mHz break is validated from two different detectors LAXPC20 and SXT, consistent with each other within errorbars. It can be clearly seen that the break for 2019 observation is detected at a higher frequency than 2017 observation with both the fittings. Also, the break frequency obtained with Lorentzian fitting is twice as higher than those obtained with broken power-law fitting.

The band-limited noise is observed to be weaker during the 2019 observation with $N_{Bkn}=6.09$ as compared to 2017 observation with $N_{Bkn}=16.08$. Detection of breaks at such low flux is in accordance with the result obtained by Plant et al. (2015) where RXTE observations of GX 339-4 in hard (rise) as well as hard (decay) states exhibited mHz break frequencies in the PDS. The unabsorbed flux level of these observations was in the range $0.82 - 59.6 \times 10^{-10} \text{ erg s}^{-1} \text{ cm}^{-2}$. They used the XSPEC model *Phabs*Powerlaw* to fit the photon spectrum and found the photon index to be 1.565, which is also closer to the photon index we have found for our observations. Furthermore, for their lowest flux observation a truncation radius of $79 R_g$ was estimated for reflection component *Relline*. Also, these observations show a trend in break frequency moving towards higher frequency from 2.55 to 195 mHz with the increasing flux. As men-

Figure 4. The fitting of νP_ν curve with broken power-law model for (A) LAXPC10 (B) LAXPC20 (C) LAXPC10 + LAXPC20 (D) SXT for 2017 observation and (A') LAXPC20 and (B') SXT for 2019 observation.

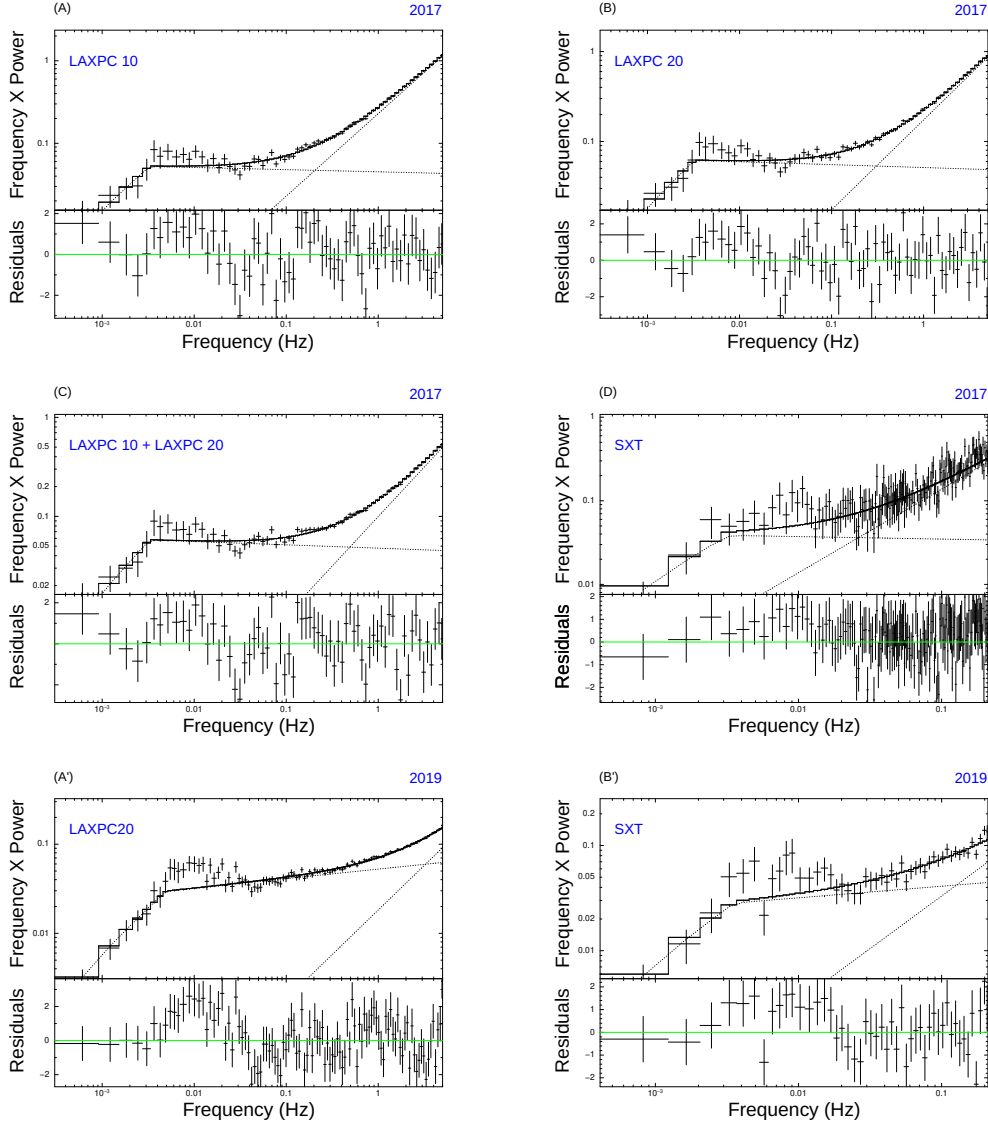
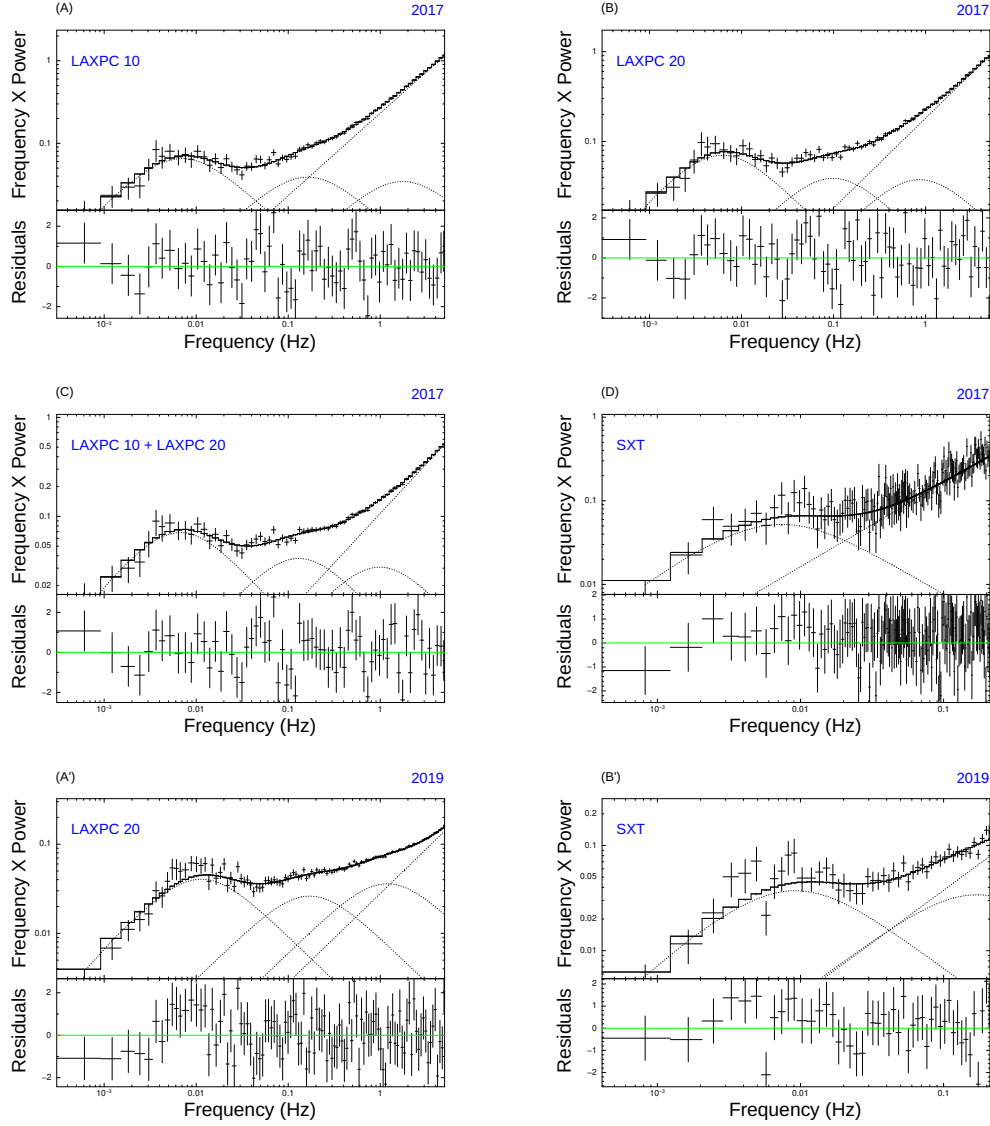


Table 2. Best fit parameters estimated with broken power-law fitting of PDS for 2017 and 2019 observations

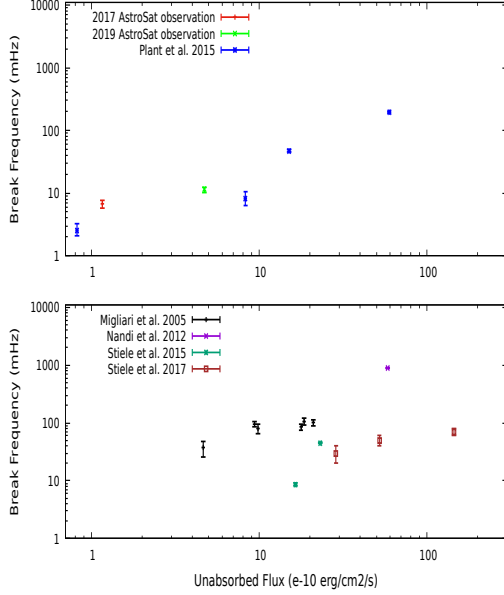
BROKEN POWER-LAW FITTING						
Observation	Payload	ν_{brk} (mHz)	N_{Bkn}	P_2	N_{noise}	χ^2/dof
2017	LXP10	$3.25^{+0.83}_{-0.76}$	$16.08^{+0.52}_{-0.52}$	$1.027^{+0.011}_{-0.011}$	$0.2292^{+0.0017}_{-0.0017}$	86.67/66.00=1.31
	LXP20	$3.22^{+0.80}_{-0.68}$	$19.16^{+0.53}_{-0.53}$	$1.033^{+0.01}_{-0.009}$	$0.1700^{+0.0010}_{-0.0010}$	91.92/66.00 = 1.39
	LXP10+20	$3.28^{+0.79}_{-0.67}$	$17.66^{+0.41}_{-0.41}$	$1.034^{+0.008}_{-0.008}$	$0.0997^{+0.0009}_{-0.0009}$	92.98/66.00=1.41
	SXT	$3.19^{+1.77}_{-1.03}$	$12.11^{+5.01}_{-4.31}$	$1.034(f)$	$1.38^{+0.12}_{-0.12}$	125.92/141.00=0.89
2019	LXP20	$4.87^{+0.91}_{-0.78}$	$6.09^{+0.082}_{-0.082}$	$0.893^{+0.012}_{-0.012}$	$0.0183^{+0.0004}_{-0.0004}$	180.99/102.00=1.77
	SXT	$3.53^{+1.46}_{-0.94}$	$8.05^{+2.38}_{-2.12}$	$0.893(f)$	$0.33^{+0.05}_{-0.05}$	49.88/46.00=1.08

Notes : P_1 was fixed at zero.

Figure 5. The fitting of νP_ν curve with multi-Lorentzian model for (A) LAXPC10 (B) LAXPC20 (C) LAXPC10 + LAXPC20 (D) SXT for 2017 observation and (A') LAXPC20 and (B') SXT for 2019 observation.**Table 3.** Best fit parameters estimated with multi-Lorentzian fitting of PDS for 2017 and 2019 observations

LORENTZIAN FITTING									
Observation	Payload	ν_{L1} (mHz)	N_{L1}	ν_{L2} (Hz)	N_{L2}	ν_{L3} (Hz)	N_{L3}	N_{noise}	χ^2/dof
2017	LXP10	$6.95^{+1.11}_{-0.93}$	$0.21^{+0.02}_{-0.02}$	$0.16^{+0.03}_{-0.03}$	$0.12^{+0.01}_{-0.01}$	$1.75^{+1.16}_{-0.64}$	$0.11^{+0.06}_{-0.028}$	$0.232^{+0.008}_{-0.008}$	$63.48/63.00=1.01$
	LXP20	$6.12^{+1.10}_{-0.93}$	$0.22^{+0.03}_{-0.03}$	$0.196^{+0.054}_{-0.043}$	$0.12^{+0.01}_{-0.01}$	$0.86^{+0.29}_{-0.19}$	$0.118^{+0.013}_{-0.014}$	$0.182^{+0.002}_{-0.003}$	$83.67/63.00=1.33$
	LXP10+20	$6.65^{+1.09}_{-0.92}$	$0.22^{+0.02}_{-0.02}$	$0.13^{+0.026}_{-0.024}$	$0.12^{+0.01}_{-0.01}$	$0.98^{+0.28}_{-0.20}$	$0.097^{+0.010}_{-0.011}$	$0.107^{+0.002}_{-0.002}$	$76.43/63.00=1.21$
	SXT	$7.34^{+2.03}_{-1.51}$	$0.16^{+0.03}_{-0.03}$	$0.13(f)$	< 0.05	—	—	$1.63^{+0.09}_{-0.09}$	$114.32/140.00=0.82$
2019	LXP20	$11.40^{+1.07}_{-1.08}$	$0.13^{+0.01}_{-0.01}$	$0.17^{+0.02}_{-0.02}$	$0.821^{+0.006}_{-0.06}$	$1.19^{+0.12}_{-0.10}$	$0.11^{+0.005}_{-0.005}$	$0.0280^{+0.0005}_{-0.0005}$	$114.80/99.00=1.16$
	SXT	$10.95^{+2.56}_{-1.87}$	$0.13^{+0.02}_{-0.02}$	$0.17(f)$	$0.107^{+0.063}_{-0.064}$	—	—	$0.598^{+0.034}_{-0.034}$	$44.760/45.000=0.997$

Figure 6. Variation in break frequency (mHz) with flux ($10^{-10} \text{ erg s}^{-1} \text{ cm}^{-2}$) as plotted for Plant et al. 2015 and this work (Upper Panel) and for values obtained by Migliari et al. 2005, Nandi et al. 2012, Stiele et al. 2015 and Stiele et al. 2017 (Lower Panel).



tioned in section 4.2, we also include points from previous hard state observations of GX 339-4 (Figure 6) and find that our values roughly fit in the evolution of break frequency with flux as seen in different observations of GX 339-4.

This evolution of break frequency is according to the truncated disk model (Done et al. (2007); Ingram & Done (2011) and references therein). In this model, low L/L_{edd} state has a truncated accretion disk at a certain radius (R_{in}) after which the disk is replaced by a geometrically thicker and optically thinner hot inner flow (or corona) (Rózańska & Czerny 2000; Mayer & Pringle 2007). The spectral transitions in this model are attributed to the modification of the geometry of accretion disk and corona. Also, this model associates the characteristic frequencies in the PDS with frequencies of the two flows. For *e.g.*, the lowest characteristic frequency (ν_{brk}) in the PDS of black hole binaries is associated with the viscous time scale (Churazov et al. 2001; Gilfanov & Arefiev 2005) at the truncation radius of the accretion disk (or the outer edge of the hot inner flow), which is since at the truncation radius of the disk the viscous time scale is much greater than the thermal or dynamic time scales (Frank et al. 2002). With the source evolving to higher luminosity states, the truncation radius approaches the ISCO. Therefore, with this geometrical change all characteristic frequencies in the PDS are expected to move to higher frequencies. Figure 6 shows a similar behaviour where the break frequency is seen to evolve with the flux. In addition to this Plant et al. (2015) have observed the evolution of truncation radius with the luminosity which has been also observed in Tomsick et al. (2009) and many other works which is also in line with the truncated disk model.

As already mentioned above, the characteristic low-frequency break can be associated with the viscous time scale (t_{visc}) at the truncation radius of the accretion disk, as per the truncated disk model. The expression for viscous time scale for a standard accretion disk is given as (Frank et al. 2002; Done et al. 2007),

$$t_{\text{visc}} = 4.5 \times 10^{-3} \frac{1}{\alpha} \left(\frac{H}{R} \right)^{-2} \left(\frac{R}{6 R_g} \right)^{3/2} \left(\frac{M}{10 M_{\odot}} \right) \quad (1)$$

Here, α is the dimensionless viscosity parameter as prescribed in Shakura & Sunyaev (1973), H/R is the semi-thickness of the disk, R_g is the gravitational radius and M is the mass of the compact object.

Using this expression of viscous timescale, we have estimated the value of truncation radius for both our observations. For 2017 observation (LAXPC20), we have $t_{\text{visc}} = t_{\text{brk}} = 1/\nu_{\text{brk}} = 163.4\text{s}$ whereas for 2019 observation (LAXPC20) we have $t_{\text{visc}} = 87.7\text{s}$. After putting these values in equation 1 with $\alpha = 0.1$ and $H/R = 0.1$ (parameters for a thin accretion disk) and mass of black hole = $6M_{\odot}$, we estimated R_{in} to be $92.5 R_g$ and $61.08 R_g$ for 2017 and 2019 observation respectively. As per these values R_{in} is found to be closer to the ISCO for 2019 observation than 2017 observation. These estimated values are close to the value of inner radius fixed for model component *Relline* *i.e.* $R_{\text{in}} = 100 R_g$ and to the value Plant et al. (2015) obtained for their lowest flux observation ($R_{\text{in}} = 79 R_g$).

To conclude the results, we observed mHz breaks in the PDS of GX 339-4 for two different observations of its faint low/hard state. We confirm these mHz detections with independent detectors (LAXPCs and SXT). These breaks are also few of the lowest frequency breaks observed for this source which may have a connection with very low flux of these observations. The comparison of these low-frequency breaks with breaks observed for few other low hard state observations imply that both our observations nearly fit in the evolution of the break frequency with source flux, which is in line with the truncated disk model. However, the spectral fitting shows that few spectral parameters were not constrained properly, therefore modelling data with better spectral resolution data such as from NuSTAR can result in finding better constraint on these parameters including the truncation radius. Also, long exposures of the source with for *e.g.* SWIFT/XRT or NICER could provide better spectral modelling.

6 ACKNOWLEDGEMENT

NH is grateful to the LAXPC and SXT teams for providing the data and requisite software tools for the analysis. NH is also grateful to the Inter-University Centre for Astronomy and Astrophysics (IUCAA) for allowing frequent visits to work on this project. NH acknowledges the funding received from the Department of Science and Technology (DST) under the scheme of INSPIRE fellowship.

7 DATA AVAILABILITY

AstroSat data analysed in this work can be accessed through the Indian Space Science Data Center (ISSDC) website (<https://astrobrowse.issdc.gov.in/astroarchive/archive/Home.jsp>). The data was analysed with the packages of HEASoft version (6.26.1) (<https://heasarc.gsfc.nasa.gov/docs/software/heasoft/>). The softwares used for LAXPC and SXT data reduction are available on <http://astrosat-ssc.iucaa.in/?q=laxpcData> and [http://www.tifr.res.in/~astrosat/\\$sxt/dataanalysis.html](http://www.tifr.res.in/~astrosat/$sxt/dataanalysis.html), respectively.

REFERENCES

- Agrawal P., et al., 2017a, *Journal of Astrophysics and Astronomy*, 38, 30
- Agrawal P., et al., 2017b, *Journal of Astrophysics and Astronomy*, 38, 30
- Belloni T., 2006, *Advances in Space Research*, 38, 2801
- Belloni T. M., 2010, in , *The Jet Paradigm*. Springer, pp 53–84
- Belloni T., Hasinger G., 1990, *Astronomy and Astrophysics*, 227, L33
- Belloni T., Mendez M., Van Der Klis M., Hasinger G., Lewin W., Van Paradijs J., 1996, *The Astrophysical Journal Letters*, 472, L107
- Belloni T., Psaltis D., Van der Klis M., 2002, *The Astrophysical Journal*, 572, 392
- Belloni T., Homan J., Casella P., Van Der Klis M., Nespoli E., Lewin W., Miller J., Méndez M., 2005, *Astronomy & Astrophysics*, 440, 207
- Casella P., Belloni T., Stella L., 2005, *The Astrophysical Journal*, 629, 403
- Churazov E., Gilfanov M., Revnivtsev M., 2001, *Monthly Notices of the Royal Astronomical Society*, 321, 759
- Dauser T., Wilms J., Reynolds C., Brenneman L., 2010, *Monthly Notices of the Royal Astronomical Society*, 409, 1534
- Done C., Gierliński M., Kubota A., 2007, *The Astronomy and Astrophysics Review*, 15, 1
- Dunn R., Fender R., Körding E., Belloni T., Cabanac C., 2010, *Monthly Notices of the Royal Astronomical Society*, 403, 61
- Fabian A., Rees M., Stella L., White N. E., 1989, *Monthly Notices of the Royal Astronomical Society*, 238, 729
- Ford E. C., van der Klis M., Méndez M., van Paradijs J., Kaaret P., 1998, *The Astrophysical Journal Letters*, 512, L31
- Frank J., King A., Raine D., et al., 2002, *Accretion power in astrophysics*. Cambridge university press
- Gandhi P., Altamirano D., Russell D. M., Knigge C., Middleton M., Veledina A., Beri A., Paice J., 2017, *The Astronomer's Telegram*, 10798, 1
- Gilfanov M., 2010, in , *The Jet Paradigm*. Springer, pp 17–51
- Gilfanov M., Arefiev V., 2005, arXiv preprint astro-ph/0501215
- Heida M., Jonker P., Torres M., Chiavassa A., 2017, *The Astrophysical Journal*, 846, 132
- Homan J., Belloni T., 2005, in , *Astrophysics and Space Science*. Springer, pp 107–117
- Hynes R. I., Steeghs D., Casares J., Charles P., O'Brien K., 2004, *The Astrophysical Journal*, 609, 317
- Ingram A., Done C., 2011, *Monthly Notices of the Royal Astronomical Society*, 415, 2323
- Laor A., 1991, in , *Iron Line Diagnostics in X-ray Sources*. Springer, pp 205–208
- Magdziarz P., Zdziarski A. A., 1995, *Monthly Notices of the Royal Astronomical Society*, 273, 837
- Markert T., Canizares C., Clark G., Lewin W., Schnopper H., Sprott G., 1973, *The Astrophysical Journal*, 184, L67
- Mayer M., Pringle J., 2007, *Monthly Notices of the Royal Astronomical Society*, 376, 435
- Méndez M., Belloni T., van der Klis M., 1998, *The Astrophysical Journal Letters*, 499, L187
- Migliari S., Fender R., Van Der Klis M., 2005, *Monthly Notices of the Royal Astronomical Society*, 363, 112
- Miyamoto S., Kitamoto S., Iga S., Negoro H., Terada K., 1992, *The Astrophysical Journal*, 391, L21
- Nandi A., Debnath D., Mandal S., Chakrabarti S. K., 2012, *Astronomy & Astrophysics*, 542, A56
- Nowak M. A., 2000, *Monthly Notices of the Royal Astronomical Society*, 318, 361
- Nowak M. A., Vaughan B. A., Wilms J., Dove J. B., Begelman M. C., 1999a, *The Astrophysical Journal*, 510, 874
- Nowak M. A., Wilms J., Dove J. B., 1999b, *The Astrophysical Journal*, 517, 355
- Oda M., Gorenstein P., Gursky H., Kellogg E., Schreier E., Tananbaum H., Giacconi R., 1971, *The Astrophysical Journal*, 166, L1
- Plant D., Fender R., Ponti G., Muñoz-Darias T., Coriat M., 2015, *Astronomy & Astrophysics*, 573, A120
- Radhika D., Ramadevi M., Seetha S., 2014, arXiv preprint arXiv:1401.1135
- Rao A., Gandhi P., Russell D. M., Motta S., Lewis F., Paice J. A., 2019, *The Astronomer's Telegram*, 13024, 1
- Róžańska A., Czerny B., 2000, *Monthly Notices of the Royal Astronomical Society*, 316, 473
- Russell D. M., Lewis F., Gandhi P., 2017a, *The Astronomer's Telegram*, 10797, 1
- Russell T. D., Tetarenko A. J., Sivakoff G. R., Miller-Jones J. C. A., 2017b, *The Astronomer's Telegram*, 10808, 1
- Shakura N. I., Sunyaev R. A., 1973, *Astronomy and Astrophysics*, 24, 337
- Singh K., et al., 2017, *Journal of Astrophysics and Astronomy*, 38, 29
- Stiele H., Kong A., 2017, *The Astrophysical Journal*, 844, 8
- Stiele H., Yu W., 2015, *Monthly Notices of the Royal Astronomical Society*, 452, 3666
- Sunyaev R., Trümper J., 1979, *Nature*, 279, 506
- Thorne K., Price R., 1975, *The Astrophysical Journal*, 195, L101
- Titarchuk L., Shaposhnikov N., Arefiev V., 2007, *The Astrophysical Journal*, 660, 556
- Tomsick J. A., Yamaoka K., Corbel S., Kaaret P., Kalemci E., Migliari S., 2009, *The Astrophysical Journal Letters*, 707, L87
- Van der Klis M., 1989, in , *Timing neutron stars*. Springer, pp 27–69
- Wijnands R., van der Klis M., 1999, *The Astrophysical Journal*, 514, 939
- Yadav J., et al., 2016, in *Space Telescopes and Instrumentation 2016: Ultraviolet to Gamma Ray*. p. 99051D
- Zdziarski A. A., Ziółkowski J., Mikołajewska J., 2019, *Monthly Notices of the Royal Astronomical Society*, 488, 1026